PHYSICAL REVIEW C VOLUME 50, NUMBER 4 OCTOBER 1994

ARTICLES

Multinucleon effects in muon capture on ^{3}He at high energy transfer

S. E. Kuhn,* W. J. Cummings,† G. E. Dodge,‡ S. S. Hanna, and B. H. King
Stanford University, Stanford, California 94305

Y. M. Shin
University of Saskatchewan, Saskatoon, Saskatchewan, Canada S7N 0W0

J. G. Congleton,§ R. Helmer, R. B. Schubank, N. R. Stevenson, and U. Wienands‖
TRIUMF, Vancouver, British Columbia, Canada V6T 2A3

Y. K. Lee
The Johns Hopkins University, Baltimore, Maryland 21218

G. R. Mason
University of Victoria, Victoria, British Columbia, Canada V8W 3P6

B. E. King
Simon Fraser University, Burnaby, British Columbia, Canada V5A IS6

K. S. Chung and J. M. Lee
Yonsei University, Seoul 120-749, Korea

D. P. Rosenzweig
University of Washington, Seattle, Washington 98195

(Received 27 December 1993)

Energy spectra of both protons and deuterons emitted following the capture of negative muons by ^{3}He nuclei have been measured for energies above 15 MeV. A limited number of proton-neutron pairs emitted in coincidence were also observed. A simple plane wave impulse approximation (PWIA) model calculation yields fair agreement with the measured proton energy spectra, but underpredicts the measured rate of deuteron production above our energy threshold by a large factor. A more sophisticated PWIA calculation for the two-body breakup channel, based on a realistic three-body wave function for the initial state, is closer to the deuteron data at moderate energies, but still is significantly lower near the kinematic end point. The proton-neutron coincidence data also point to the presence of significant strength involving more than one nucleon in the capture process at high energy transfer. These results indicate that additional terms in the capture matrix element beyond the impulse approximation contribution may be required to explain the experimental data. Specifically, the inclusion of nucleon-nucleon correlations in the initial or final state and meson exchange current contributions could bring calculations into better agreement with our data. A fully microscopic calculation would thus open the possibility for a quantitative test of multinucleon effects in the weak interaction.

PACS number(s): 23.40.Hc, 25.10.+s, 27.10.+h

I. INTRODUCTION

Nuclear muon capture $Z+\mu^- \rightarrow (Z-1)^*+\nu_\mu$ normally leads to the emission of an energetic neutrino carrying most of the rest energy of the muon, while the energy transfer to the nucleus $q^0 = m_\mu - E_\nu$ is relatively small. The transferred energy leads to low-lying excitations of the residual nucleus up to the giant resonant region [1] or to the emission of medium energy neutrons (see, e.g., Ref. [2] and references therein). These conditions can be understood in the impulse approximation (IA) picture, in

---

*Present address: Old Dominion University, Norfolk, VA 23529.

†Present address: TRIUMF, Vancouver, British Columbia, Canada V6T 2A3.

‡Present address: Vrije Universiteit, 1081HV Amsterdam, The Netherlands.

§Present address: Instituut voor Theoretische Fysica, Postbus 80.006, 3508 TA Utrecht, The Netherlands.

‖Present address: Stanford Linear Accelerator Center, Stanford, CA 94309.

0556-2813/94/50(4)/1771(16)/$06.00

which the muon is absorbed by a single proton moving with relatively low momentum (of the order of the Fermi momentum) inside the nucleus. Typically, more than 90% of the total capture rate can be attributed to this "quasifree" kinematic regime [3,4].

On the other hand, there have been a number of experiments [5–16] which observed muon capture events leading to large excitation energies and thus large energy transfers to the recoil nuclei. These large excitation energies reveal themselves in a variety of final-state channels: high energy neutron emission [5–8,16], high energy proton emission [9–14], and fission [15]. While the observation of high energy neutrons (beyond 40 MeV) could in principle be attributed to the presence of high momentum components in the initial nuclear wave function (in excess of 300 MeV/c), the other observed channels hint strongly of the existence of capture processes involving more than one nucleon. Such nucleon pair correlations in either the initial- or final-state wave function and meson exchange current (MEC) contributions in the capture process could be responsible for the observed strength at large q^0.

Lifshitz and Singer [17] have studied the importance of MEC for muon capture in extreme kinematics, i.e., at high energy transfer, in medium to heavy nuclei. Their approach takes into account several MEC diagrams which they evaluate using a simple Fermi-gas model to obtain the nuclear wave function. They include the effects of final-state interactions using a hybrid exciton model. Their calculated energy spectra for high energy proton emission agree qualitatively with existing experimental data, and they reproduce the observed emission probability for protons above 40 MeV for Si, Mg, and Pb within a factor of 2. This result can be interpreted as a strong indication of the importance of MEC in this extreme kinematic regime, since the predicted contribution from the IA is negligible in this region, according to Ref. [17]. On the other hand, it is difficult to quantify the relative importance of different MEC diagrams and nucleon pair correlations for the high energy capture rate in heavier nuclei, since there are no reliable microscopic wave functions and final-state interactions make the interpretation of experimental results doubtful.

A different approach to this problem was employed by Bernabéu, Ericson, and Jarlskog [18]. These authors used the conserved vector current (CVC) hypothesis and the partially conserved axial-vector current (PCAC) hypothesis, together with the assumption of axial locality, to relate muon capture on nuclei to s- and p-wave pion absorption and photonuclear reactions. This approach avoids the uncertainties in the nuclear wave functions, since the muon capture rates are expressed in terms of experimental quantities, such as the complex pion scattering lengths, which already contain the influence of the nuclear dynamics. In addition, MEC effects and nucleon-nucleon correlations are included "automatically" since they dominate pion capture. Unfortunately, the results of Ref. [18] can only be applied to the kinematic end point of zero neutrino energy, which makes a comparison with experiment less direct. Also, since the dynamics of both muon capture and pion capture are not derived, but merely related to each other in this model, direct inferences cannot be drawn on the microscopic structure of the capture process.

For a clear comparison between theory and experiment, it is necessary to study muon capture in few-body ($A \leq 3$) nuclei, where microscopic calculations of both the initial- and final-state wave functions are feasible. Detailed theoretical calculations for muon capture on deuterons [19,20] show that the explicit inclusion of MEC in the capture matrix element enhances the calculated capture rate near the kinematic end point by a large factor relative to the contribution from high momentum components in the deuteron wave function. The available data for this deuteron capture process [16] indicate the existence of such an enhancement, but the results are somewhat inconclusive because of limited statistics and large background uncertainties.

In this paper we report the final results of the first measurement of muon capture at high energy transfer in ^{3}He. Specifically, we observed fast protons both as singles and in coincidence with neutrons in the reaction

$$\mu^- + {}^3\text{He} \rightarrow p + n + n + \nu_\mu \tag{1}$$

and also energetic deuterons in the reaction

$$\mu^- + {}^3\text{He} \rightarrow d + n + \nu_\mu \ . \tag{2}$$

Preliminary results from this measurement have been published [21].

One advantage of using ^{3}He as the target lies in the fact that there are charged particles in the final state that can be observed with high efficiency and good background suppression. On the theoretical side there has been rapid progress recently on the development of reliable three-body wave functions for the initial state and for the breakup channels of the final state in the $A = 3$ system [22]. These wave functions could be used to calculate the capture rates exactly for comparison with our experimental data.

In the following sections we describe in detail our experimental setup (Sec. II), our Monte Carlo simulation of that setup (Sec. III), and the data analysis (Sec. IV). Possible background contributions are discussed in Sec. V. In Sec. VI we present our results for reactions (1) and (2) and compare them with simple model calculations. We also compare our deuteron data to the prediction of the method of Bernabéu, Ericson, and Jarlskog [18] and to our own PWIA calculation for the deuteron spectrum which is based on a realistic three-body wave function of the ^{3}He ground state.

II. EXPERIMENTAL SETUP

Figure 1 shows an overview of the experimental setup and Fig. 2 shows the target and the charged particle telescopes in more detail. We now describe each component of the experiment.

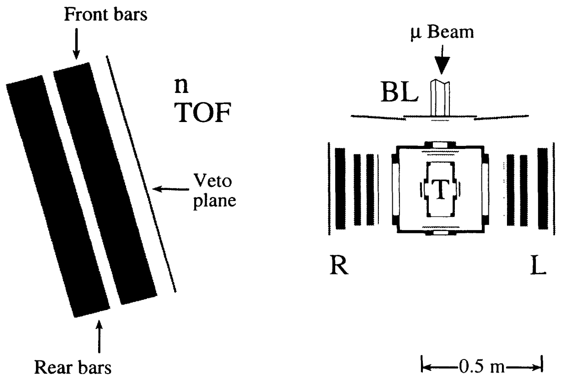

FIG. 1. Overview of the experimental setup. This figure shows the relative spatial arrangement of the beam line (BL), target (T), left (L), and right (R) charged particle telescopes, and the neutron time-of-flight detector (n TOF).

A. Muon beam

The muons used for this experiment were supplied by the secondary channel M9B at the TRI-University Meson Facility (TRIUMF) in Vancouver, Canada. This channel consists of a thick Be production target on which the primary 500 MeV proton beam impinges, a pion extraction system, a superconducting solenoid where the pions decay into muons, and a muon momentum analyzing magnet and optical system. For our experiment, an additional collimator was introduced into this beam line at a point of high dispersion to reduce the momentum width of the beam. We also established a new chromatic tune for this channel to increase the momentum resolution. We measured the full momentum distribution of the beam using the stopping method and found a centroid of 43 MeV/c and a full width at half maximum of only 6%. In addition, we measured the spatial distribution of the muon beam as important input information for our Monte Carlo simulation. The narrow momentum collimation resulted in a fairly low beam particle rate of roughly 14 kHz. The fraction of electrons in the beam was about 20% and we determined an upper limit of 10^{-3} for the pion contamination.

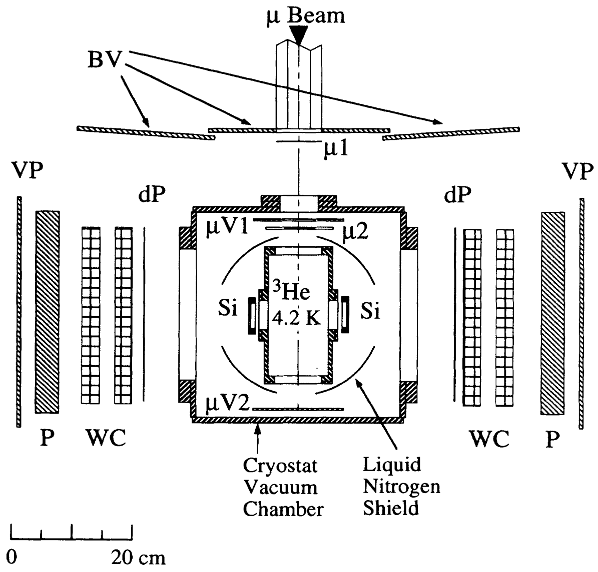

FIG. 2. Detailed view of the target cryostat chamber and charged particle telescopes. $\mu1$, $\mu2$, μV1, and μV2 are the beam telescope detectors (plastic scintillators), and BV are additional beam veto counters. Si, dP, P, and VP are the silicon surface barrier detectors, thin ("ΔE") and thick ("E") scintillator detectors and the veto scintillator detectors, respectively. WC are the delay line wire chambers. For further explanation see text.

Periodically we tuned the muon channel to maximize the flux of pions at a momentum that would allow them to reach our target. This was done for calibration purposes and to check out the electronics and triggers. Periodically, throughout the experiment we also measured cosmic-ray events and background from the main beam line while no muons were transported to the experimental area.

B. Beam counters

Beam particles leaving the M9B beam line were detected by a set of plastic scintillator beam counters (Fig. 2). The first counter $\mu1$, 0.8 mm thick, covered the aperture of the "beam snout" and detected all particles exiting the beam line. A set of beam veto scintillator counters (BV) was used to detect far off-axis beam particles that might have created background signals in the charged particle telescopes (Sec. II D). Inside the target cryostat there were three more counters: $\mu2$, a 5 cm diameter scintillator disc embedded in a Lucite light guide which detected and identified (via pulse height) muons, pions, and electrons moving toward a fiducial region within the target; μV1, a 3.2 mm thick scintillator with a 5 cm hole in the center which was used to veto off-axis beam particles; and μV2 which allowed us to detect penetrating electrons and to determine the stopping distribution of the muons.

C. Target cryostat

The target consisted of a copper cell, 10 cm in diameter by 23 cm long (see Fig. 2), filled with ^{3}He gas at a pressure of 1 atmosphere. The cell was in thermal contact with a liquid helium bath and was surrounded by a heat shield at liquid nitrogen temperature, so that the ^{3}He gas was at 4.2 K and had a density of 11 mg/cm^3. To allow muons to enter and exit the cell, an 8 cm diameter window made of 76 μm aluminum foil was provided at each end of the cell. For the reaction products, a 5 cm diameter port made of 12.5 μm HAVAR$^{\text{TM}}$ foil was inserted in both sides of the cell. All inner surfaces of the target cell were covered by 0.1 mm lead foil to make sure that muons stopping in the target walls would capture quickly in a high-Z material.

The target and the heat shield, along with the first charged particle detectors, were contained in a vacuum vessel equipped with a muon entrance window made of 76 μm thick aluminum foil and two 20 cm diameter particle exit ports of 254 μm Mylar$^{\text{TM}}$ covered by 25 μm Tedlar$^{\text{TM}}$ (to make the ports opaque).

D. Charged particle detectors

The charged reaction products which exited the target through its two exit ports were detected by several detectors which constituted two charged particle telescopes. Although these telescopes had the same set of detector elements, their performances turned out to be somewhat different. Section IV explains how the signals in these detector elements were used for event selection and analysis.

As shown in Fig. 2, the first detector to be traversed by each charged particle was an internal silicon detector, 4.2 cm in diameter by 240 μm thick, operated at a temperature of 77 K (liquid nitrogen). The energy loss signal in this detector was used for particle identification and as a tag for particles emerging from the target itself instead of from other surrounding material. The silicon detectors were position sensitive and were designed and built at Lawrence Berkeley Laboratory for this experiment.

The next detector reached by the charged particles, just outside the vacuum chamber, was a thin plastic scintillator (BC408) detector dP, 1 mm thick by 30 cm×30 cm square. Medium energy protons and all but the highest energy (above 24 MeV) deuterons were stopped in this detector. For penetrating protons, deuterons, and electrons this detector yielded a second measurement of their energy loss.

After the dP detector came two 30 cm×30 cm delay-line wire chambers (standard TRIUMF equipment). Each wire chamber measured both the x and the y coordinates of each charged particle, allowing one to trace back the particle trajectory to the target. These wire chambers were followed by a 35 mm thick plastic scintillator (BC408) detector P with an area of 35 cm×35 cm, which stopped all the remaining protons and deuterons coming from muon capture events. This detector was used to determine the total energy of the detected nuclear particles. Most electrons passed through this detector and were tagged by a 6.4 mm thick plastic scintillator detector VP placed immediately behind it.

The acceptance of each telescope was constrained by the aperture of its silicon detector to roughly 0.09 sr (0.7% of 4π). The overall proton detection efficiency was $\cong$90%.

E. Neutron detector

Neutrons were detected by an array of 14 plastic scintillator bars. Each bar was 15 cm×15 cm×105 cm long. Seven horizontal bars were stacked vertically in front and seven behind to give a scintillator volume of roughly 1 m×1 m×0.3 m. Three thin planar scintillator detectors in front of this array were used to veto charged particles. Additional details of this array are described in Ref. [23]. In our experiment the neutron detector was positioned at an average distance of 150 cm from the target center and covered an angular range of 73° to 110° with respect to the muon beam line. The somewhat unusual orientation shown in Fig. 1 was mandated by space constraints.

Each scintillator bar was viewed by a phototube at each end. The threshold of each tube was set at approximately 3 MeV electron equivalent (MeV el. eq.), to suppress counts from gamma rays and other background. Extensive simulations were run with an in-house code developed for this detector to determine the neutron detection efficiency. The average efficiency over the energy range of interest, 10 MeV–90 MeV, was calculated to be 28%. A measurement of the efficiency at 90 MeV agreed with the simulation within 10%.

III. MONTE CARLO

We developed an extensive Monte Carlo simulation of the experimental apparatus and detector response for several purposes: calibration of the detectors, unfolding of measured spectra, and estimates for both signal and background count rates. In the following we describe different aspects of this Monte Carlo program.

A. Stopping distribution

The first part of the Monte Carlo program was developed to calculate the spatial distribution of muons stopped in the target, depending on which of the beam detectors they had traversed. The program started out with the measured spatial, angular, and momentum distributions of the beam and followed a random sample of 10^5 typical muons through all constituents of the experimental apparatus until their energies were below 1 keV. The deceleration of the muons was modeled with the aid of energy-range curves for muons in all materials encountered [24]. Multiple scattering of the muons was simulated with a new algorithm that combines the full Molière distribution for small angles and the Rutherford scattering law for larger angles [25]. Since the momentum range achieved was very narrow, most muons stopped within the gas volume of the target (81% according to the simulation); the remainder stopped either in one of the beam counters or in the target wall. Of all the muons producing signals in $\mu 1$ and $\mu 2$ and no signal in $\mu V1$ or $\mu V2$, only 3% stopped in the side walls of the target, the other 97% stopping in the ^{3}He gas volume.

We checked the accuracy of our calculated spatial distribution by comparing the measured traceback distribution of electrons from muon decay (obtained with wire chamber information) with the corresponding simulated distribution. Figure 3 shows the measured and

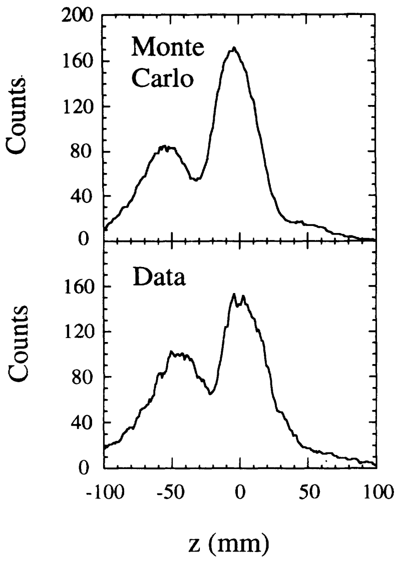

FIG. 3. Measured (lower panel) and simulated (upper panel) traceback distribution for electrons from muon decay (Michel electrons) in arbitrary units. The flight path of each measured or simulated Michel electron is projected back to the plane containing the Si detector; the distributions are plotted in this plane. The z axis is the distance along the beam direction from the center of the target. The central peak corresponds to muons that stopped in the center of the target and the broader structure at negative z is due to lower momentum muons stopping early in the target volume (see text).

the simulated distributions; the central peak corresponds to muons that stopped in the center of the target and the broader structure is due to lower momentum muons stopping early in the target volume (see Sec. III D). The agreement seen in Fig. 3 is quite good; it was optimized by using an average muon momentum of 42.4 MeV/c in the Monte Carlo simulation instead of the measured value of 43.2 MeV/c. The total number of electrons observed in both detector arms agreed to better than 10% with the number predicted by the Monte Carlo simulation. This confirms that the total number of muons stopped within the fiducial region of the target is predicted accurately by the simulation, which is important for the overall normalization.

In addition to muon distributions we also calculated the pion distribution obtained when the channel was tuned for pions. The traceback distribution again showed fairly good agreement with the simulation, indicating that the distribution of pions within the ^{3}He volume was well described by the Monte Carlo result.

B. Secondary particles

The Monte Carlo method was also used to generate spectra of secondary particles (protons, deuterons, neutrons, and electrons) from muons or pions that stopped in the gas volume of the target, as well as for muons stopped in the target walls. The initial energy of each secondary particle was chosen according to a model distribution (see below), and the initial direction was taken at random (of course, the neutron direction was correlated to the corresponding proton direction). We then followed each particle until it was stopped either in one of the constituents of the apparatus (walls, etc.) or in a detector. We again used fits to energy-range curves and our multiple scattering algorithm to determine energy losses and multiple scattering.

For each trajectory the energy deposited in each detector was registered, as well as the x and y coordinates in each wire chamber. For the heavier secondary particles, the energy loss in the scintillators was converted to light output (in MeV el. eq.) using an empirical formula [26] that accounts for saturation effects at high ionization density in the scintillator material used in this experiment. We assumed that the response of the scintillators to electrons and that of the Si detectors to all particles were both linear. All simulated data could be "smeared" by Gaussian resolution functions. The results of each simulated event were stored in the same format as the real data and then analyzed with the same data analysis program, including identical cuts.

C. Muon capture models

To simulate the emission of protons, deuterons, and neutrons after muon capture in ^{3}He, we developed a simple PWIA model for the distributions in angle and energy of the two or three final-state nuclear fragments. This model uses the single-particle weak Hamiltonian for muon capture on a proton [2], namely,

$$H_W = \frac{G\cos\theta_C}{\sqrt{2}}\bar{\psi}_\nu[\gamma_\alpha(1+\gamma_5)]\psi_\mu\bar{\psi}_n\left[g_V\gamma^\alpha + ig_M\sigma^{\alpha\beta}\frac{q_\beta}{2m} + g_A\gamma^\alpha\gamma_5 + g_P\gamma_5\frac{q^\alpha}{m_\mu}\right]\psi_p \qquad (3)$$

and a simplified parametrization of the ^{3}He "experimental spectra function" $S(p_{\mathrm{miss}})$ for the two-body breakup and $S(p_{\mathrm{miss}}, E_{\mathrm{miss}})$ for the three-body breakup, which we take from a measurement of the reaction $^3\mathrm{He}(e,e'p)$ [27]. Here, p_{miss} and E_{miss} are the missing momentum and energy, respectively.

In the case of the two-body breakup, the deuteron is considered as a spectator in this model, with momentum

p given by p_{miss}. This ansatz yields the energy spectrum of emitted deuterons directly, after integration over the accessible phase space for the unobserved neutrino and neutron.

In order to predict proton energy spectra and joint distributions of proton and neutron variables, one has to make additional assumptions. We started again from a picture where the muon captures on a single proton, transforming it into a neutron and leaving a spectator pn pair with total momentum p_{miss} and internal energy E_{miss}. We then assumed random orientation for this pn pair relative to p_{miss} and q. Averaging over many Monte Carlo trials led to a proton energy spectrum. For the joint distribution of proton and neutron variables we considered coincidences both between the proton and the spectator neutron and between the proton and the neutron produced in the capture reaction.

For the initial energy distributions and rates of protons and deuterons emitted after muon capture on lead (the target wall material) we used a simple parametrization of the results of Krane *et al.* [11].

D. Electron simulation

For the simulation of electron events from muon decay we started out with the Michel electron energy spectrum. The electron trajectories were simulated using the same general procedure as for the heavier particles (see. Sec. III B) to ensure that the results were directly comparable. There were a few differences in the treatment of electrons compared to that of heavier particles: we used the Landau distribution at each step to calculate the electron energy loss, and we included a simple simulation of radiative losses. Also, we followed electron tracks even if they went through substantial amounts of structural material, since not all electrons were stopped by the target walls or silicon detector mounts. The simulated traceback distribution shown in Fig. 3 exhibits clearly a central peak at the position of the target exit port (around $z = 0$ mm), but there are still substantial counts outside this peak, especially upstream of the thick rim of the exit port ($z < -25$ mm).

E. Pion energy spectra

To simulate the emission of protons and deuterons after pion capture in ^{3}He, we used the energy spectra of protons and deuterons as measured by Gotta *et al.* [28]. Because of the two-body kinematics in the final state, each deuteron is emitted at a single energy of 45.3 MeV, back to back with a 87.5 MeV neutron. Protons are emitted in a continuous energy spectrum extending up to 86.1 MeV. Since the initial energy spectra are known, the resulting simulated detector signals could be used to calibrate the detector response as measured in pion runs and to test the quality of the Monte Carlo prediction.

IV. DATA ANALYSIS

A. Event selection

Events with signals in either one of the charged particle telescopes were written on tape and analyzed off-line. From this data set we extracted three subsets of charged particle events as follows.

(1) A subset of "low energy" hadronic events in either detector arm indicative of a proton or deuteron that had stopped in the dP counter. These events were defined by requiring a high ΔE signal (roughly ten times higher than minimum ionizing) from the silicon detector Si and a high E signal in dP (at least four times minimum ionizing). Through-going hadronic events were rejected by their signal in P. Figure 4 shows a two-dimensional spectrum of ΔE in Si vs E in dP for all events in the left charged particle telescope. One can clearly see the proton and the deuteron bands, very well separated from electron events in the lower left corner. At very high dP signals, around 4 MeV el. eq., both the proton and the deuteron bands break back as the particles start to penetrate dP. Thus, for the final analysis only events below 4 MeV el. eq. deposited energy in dP were considered. Only deuteron events from this subset were used in our final data set (see Sec. IV E). These deuterons had initial energies between 17 and 23 MeV.

(2) A subset of "high energy" hadronic events with signals above minimum ionizing from both the Si detector and the dP detector along with a signal above threshold in P. Two-dimensional cuts on Si vs P and on dP vs P were used to eliminate electrons from this subset of events. We also employed the time of flight from the dP to the P detector to distinguish hadronic events from electrons.

Figure 5 shows a two-dimensional plot of the time of

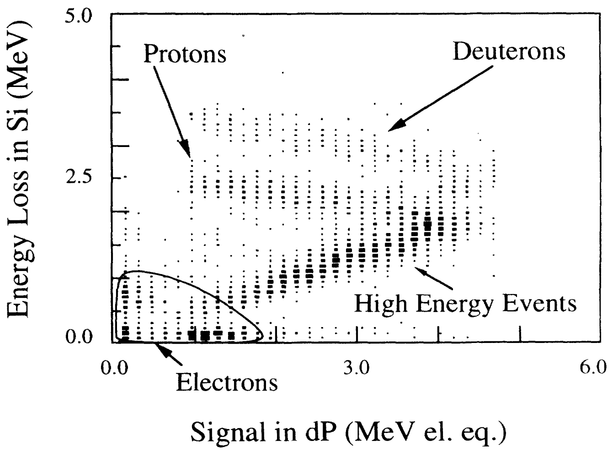

FIG. 4. Particle identification plot for protons and deuterons traversing the left charged particle telescope. Shown is the energy loss in the Si detector versus the light output (in MeV electron equivalent) of the thin dP detector. The band of deuterons stopping in dP is clearly visible.

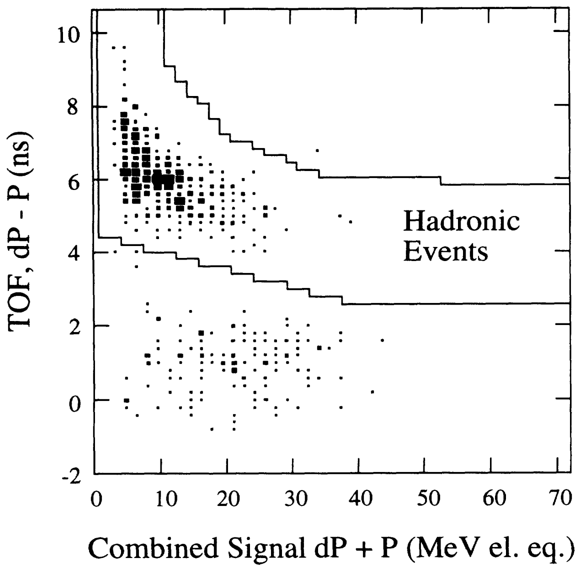

FIG. 5. Particle identification plot for the highest energy events. Shown is the time of flight (TOF) between the dP and the P detectors of the right detector arm versus the summed light output of both. All other software cuts have been applied. Hadronic events with relatively long TOF are cleanly separated from background events and electrons at shorter TOF. Those unwanted events were removed from the final data sample using the two-dimensional cut indicated in the figure.

flight (TOF) vs the sum of the signals in dP and P, already cut on the two-dimensional gates Si vs P and dP vs P. The gate shown in Fig. 5 was then used to select hadronic events. Extensive Monte Carlo simulations and comparisons with pion runs (which contained copious hadronic events, but nearly no electron events) helped to refine these cuts and determine their efficiencies. The protons contained in this sample had initial energies above 17 MeV, and the deuterons had initial energies above 25 MeV.

(3) A subset of minimum ionizing events corresponding to electrons (from muon decay) penetrating all charged particle counters. Events of this kind required a signal above threshold in all plastic scintillator detectors, including the veto counter VP. These events were prescaled by a factor 100 since muon decay is 200 times more likely than capture by ^{3}He. We used these events for detector energy calibrations and to check our overall normalization.

B. Detector calibrations

For each of the charged particle detectors we determined the energy calibration using both pion-induced hadronic events and electron events from muon decay. With our Monte Carlo program we calculated the spectrum of energy deposited in each detector for several characteristic features of the hadronic spectrum from the reactions ^{3}He(π^-,p) and ^{3}He(π^-,d) (e.g., the monoenergetic deuteron peak) and from the minimum-ionizing muon-decay electrons. These "predicted" spectra were then scaled and smeared with a Gaussian function (of width σ) until they agreed with the shape and centroid of the corresponding measured spectra. This technique yielded several calibration points for each detector which we then fitted. Figure 6 shows the result of such a fit for the left dP detector, both for the energy calibration and for the detector resolution as a function of energy. The average detector response is seen to be proportional to deposited energy, while the resolution (σ) is best fitted by a function proportional to the square root of the energy. This behavior is indicative of a resolution dominated by photon counting statistics.

The position conversion factors of the wire chambers were determined using radioactive sources at known positions and by comparing measured and predicted ranges of wire hits in the data runs. The wire chamber efficiencies were inferred by comparing coincident and singles rates from different wire chamber planes within the same telescope.

The pulse height responses from the 14 neutron counter bars were calibrated with minimum ionizing signals recorded during cosmic-ray runs. These cosmic-ray signals were also used to calibrate the relative timing of the two phototubes on each bar. The relative timing between the left charged particle detector arm and each neutron

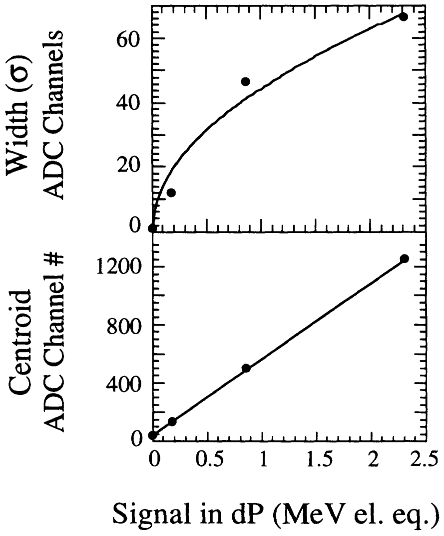

FIG. 6. Example of a detector energy calibration. The average signal magnitude in ADC channel units (lower panel) and the Gaussian width of the detector resolution (upper panel) for the left dP detectors are shown as a function of energy deposited. The four data points come from a comparison between Monte Carlo simulated and measured signals for the ADC pedestal, muon decay electrons, high energy protons from pion capture and monoenergetic deuterons from pion capture. The signal response is fitted by a straight line and the signal resolution by a least-squares fit to the square root of the energy deposited.

counter bar was determined by fitting its measured TOF distribution for the monoenergetic neutrons seen in coincidence with deuterons from $^3\mathrm{He}(\pi^-,d)n$.

C. Additional event requirements

Besides the particle identification cuts described earlier, there were several further conditions imposed on muon-induced events as follows.

To ensure that an observed event originated from a muon inside the ^{3}He target, we required that it occurred during an open muon gate. A muon gate was opened 300 ns after a "good" muon entered the target (unless a muon gate was already open) and stayed open for 4.4 μs. A "good" muon was defined by a signal above minimum ionizing in both $\mu 1$ and $\mu 2$ and no signal in μV1 and μV2. The blanking time of 300 ns was introduced to suppress events coming from muon capture on lead in the target walls and pion induced events.

Roughly 6.5% for all muons arrived during an already open muon gate and were termed "second muons." Events that occurred after a second "good" muon signal had been detected were removed from the data sample since they would distort the measurement of the muon lifetime described in Sec. IV D. The removal of these events led to a reduced "effective" lifetime of the muons of 2.11±0.02 μs, as compared to the "physical" muon life time in ^{3}He of 2.19 μs.

If there was a signal in any one of the beam counters (BV, $\mu 1$, $\mu 2$, or μV1) during a time span of 100 ns immediately preceding an event in one of the charged particle telescopes, that event was termed "prompt." Prompt events were likely to originate from pions and electrons in the secondary beam that entered the target during an open muon gate. These events were rejected.

Finally, for each penetrating charged particle with a signal in P we used the wire chamber information to calculate the point of origin, projected to the target exit port. This allowed us to remove events that came from one of the beam counters or from structural material.

D. Proton event analysis

The final proton events included in the analysis were those high energy hadronic events that passed all cuts described in Secs. IV A and IV C, plus additional cuts on the signals in the Si and dP detectors to remove deuteron events. These events were accumulated in a histogram showing the number of events versus the time elapsed since the muon stopped in the target. A maximum-likelihood fit was used to determine the lifetime of these events. The result for protons stopping in the right detector arm was $\tau = 2.16 \pm 0.17$ μs, in very good agreement with the Michel-electron result. This confirms that these events are largely free from background contributions that are random in time (which would lead to longer lifetimes), as well as from contributions from muons capturing in materials other than ^{3}He, with shorter lifetimes.

On the other hand, the lifetime for proton events in the left detector arm was significantly too long, namely, 3.04±0.25 μs, indicative of a time-independent background contribution. A maximum-likelihood analysis with the background fraction as the fitting parameter yielded a magnitude of 28% for its contribution. We describe the likely source of this background in Sec. V D. For further analysis of these left-side proton events (as well as the high-energy deuteron events), we separated the events occurring in the first half of a muon gate from those occurring in the second half. The background contribution to both sets of events should be equal, while the muon-induced events should be fewer by a factor $1/e$ in the second half. Subtraction of the second set from the first thus yields a spectrum with the background removed, but unfortunately also with a much larger statistical uncertainty.

A backfolding algorithm was used to extract the energy spectrum of protons from muon capture from the measured spectra of the P detectors in each detector arm. This algorithm was based on the fact that the Monte Carlo simulation describes rather well the observed signals of all detectors for both pion runs and proton events from muon capture (Fig. 7). We used the Monte Carlo simulation to relate the number of events within each of eight initial energy bins of 5 MeV width to the number of events observed with a given light output (in MeV el. eq.) in the P detector. We then inverted this relationship, using Bayes' theorem [29]:

$$P(A|B) = \frac{P(B|A)P(A)}{P(B)} . \tag{4}$$

Here, $P(A|B)$ is the probability that an observed proton with light output B in the P detector had been emitted

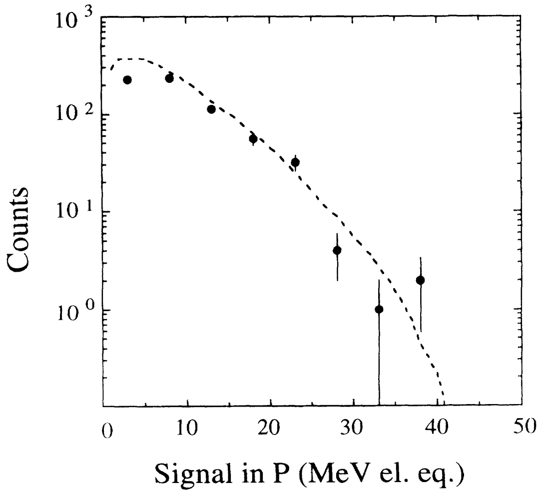

FIG. 7. Raw proton energy spectrum for the right detector arm. Shown is the number of counts versus light output signal in the P detector, binned in steps of 5 MeV electron equivalent. The dashed line is the Monte Carlo prediction.

with an initial energy in bin A, $P(B|A)$ is the likelihood that a proton with initial energy A produces a signal B in the P detector, $P(A)$ is the initial (*a priori*) energy spectrum and $P(B)$ the light output spectrum. All quantities on the right-hand side of Eq. (4) could be calculated, within our model, using the Monte Carlo simulation, and the combined quantity $\frac{P(B|A)P(A)}{P(B)}$ is rather robust against changes in the initial energy spectrum used for the simulation. Specifically, an overall change of the initial energy spectrum by an arbitrary constant factor does not change $P(A|B)$ as defined in Eq. (4) at all. Furthermore, we studied the dependence of $P(A|B)$ on the slope of the input energy spectrum and found that even a rather dramatic change (reducing the semilogarithmic slope by 35%) did not change our final proton spectrum by more than a small fraction of the statistical error. We note that such a (rather "flat") initial energy spectrum can be ruled out since it would lead to a predicted signal spectrum in the P detector incompatible with the observed spectrum (Fig. 7).

To derive the initial energy spectrum from the measured signal spectrum, one simply multiplies $P(A|B)$ by the number of observed events in each bin of light output B and sums over all bins. Figure 8 shows the resulting proton energy spectra for both detector arms, together with the initial energy distribution used in the Monte Carlo simulation.

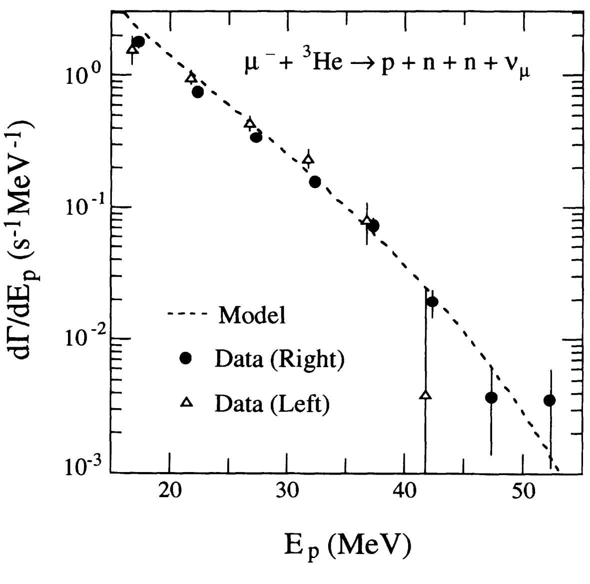

FIG. 8. Final proton energy spectrum. The partial capture rate per 1 MeV energy interval is shown, averaged over 5 MeV energy bins. The solid circles are the data from the right detector arm, while the open triangles are the data from the left detector arm (with larger error bars due to background subtraction). Both data sets are shown slightly offset from the centroid of each bin to increase legibility. Error bars are statistical only and do not contain an overall 10% normalization uncertainty. The dashed line is the prediction of the Monte Carlo model.

E. Deuteron event analysis

We were interested in two kinds of deuteron events: those with an initial energy between 17 and 23 MeV that stopped in a dP detector, and those with an energy of more than 25 MeV that left a clear signal in a P detector. The selection of high energy events was based on all the cuts described in Secs. IV A and IV C. An additional two-dimensional cut, made on the histogram of the weighted sum of energy losses in the Si and dP detectors vs the light deposited in P, separated deuteron events from proton events. The high energy deuteron data from the left side telescope were background subtracted using the method of Sec. IV D. The lower energy deuterons were selected by means of a two-dimensional cut on the Si vs dP histogram (see Fig. 4). Unfortunately, the energy resolutions of both Si and dP detectors were substantially worse for the right hand detector arm, rendering only the lower energy data in the left arm useful.

These three subsets of deuterons (high energy deuterons in both arms and low energy ones in the left arm only) could not be subdivided any further. In the case of deuterons stopping in the left dP detector, the narrow energy range accepted (a result of the small scintillator thickness of only 1 mm) was comparable to the energy smearing due to finite detector resolution and to variations in emission angle and point of origin of the deuterons within the ^{3}He gas. For the high energy events, the number of deuterons stopping in each P detector was so small that any further division would have been statistically meaningless.

For this reason we could not employ the Bayesian statistics method described in the previous section to extract the initial deuteron energy spectrum. Instead, we determined the centroid of the initial energy range contributing to each set of deuteron events passing all appropriate cuts in the Monte Carlo simulation, for several different model energy spectra. The horizontal position of each data point in Fig. 9 is the most probable energy centroid, while the horizontal error bars indicate the range of reasonable values. The vertical values are the inferred partial capture rates at that centroid energy. The vertical error bars reflect the statistical uncertainty only, while the model dependence is contained in the horizontal error bars.

F. Proton-neutron coincidences

For each left-side high-energy proton event as defined in Sec. IV D, we read out the signals from all phototubes of the 14 neutron counter bars and the 3 charged-particle veto detectors. If the signal in one neutron bar was above threshold (roughly 3 MeV el. eq.) and no signal was detected in the veto counters, the event was stored as a proton-neutron coincidence. Due to the low efficiency (28%) and limited angular acceptance of the neutron counter, only a few such coincident events were recorded. The horizontal position along the bar where the neutron arrived was determined by the time differ-

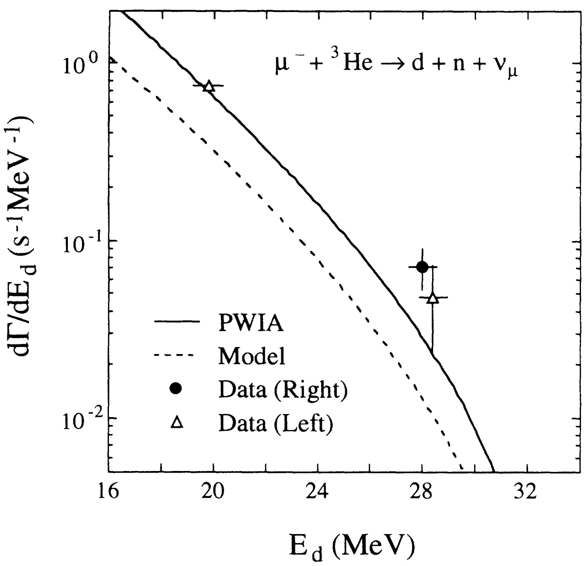

FIG. 9. Final deuteron energy spectrum. The open triangles represent deuterons stopped in dP (lower energy) and in P (high energy) in the left detector arm. The solid circle at high energy represents the deuteron data from the right P detector. The vertical error bars are the statistical uncertainties, while the horizontal error bars indicate the uncertainty of the "true" average emission energy for each data set. The dashed line is the predicted by the Monte Carlo method, while the solid line is the result of a rigorous PWIA calculation, using realistic ground-state wave functions for ^{3}He and the deuteron.

ence between the pulses in the two tubes viewing that bar, while the arrival time of the neutron was determined by the mean time of those pulses. The vertical segmentation into seven different bars provided a crude measurement of the y coordinate for each neutron.

For all coincident events we determined the approximate proton energy using a linearized relationship between measured light output in P and initial proton energy from the Monte Carlo simulation. The neutron energy was determined from the time of flight between the arrival of the coincident proton in the opposite (left) dP counter and the arrival of the neutron in its detector. To reduce our sensitivity to threshold effects at lower proton energies and to the falling efficiency of the neutron counter below 10 MeV, we discarded events with proton energy below 21 MeV and neutron energy below 10 MeV. For the remaining 29 coincident events we determined the three-momentum of the proton from its initial energy and the trajectory as measured by the wire chambers, and the (approximate) three-momentum of the neutron using the position information from the neutron counter. The sum of these two vectors yields the missing momentum p_{miss}, i.e., the sum of the momenta of the observed second neutron and the neutrino.

Due to the small number of events and the very limited region of phase space covered, we did not attempt to extract "initial" distributions of kinematic quantities. Instead, we calculated several averaged quantities from the data, e.g., the root-mean-square value, $\sqrt{\langle p^2_{\text{miss}} \rangle}$, of the missing momentum (see Sec. VI B).

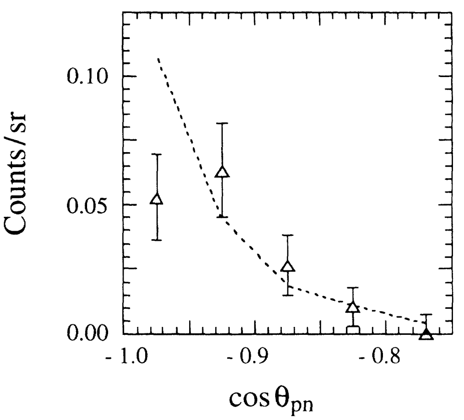

FIG. 10. Angular distribution of neutrons detected in coincidence with protons ($E_p > 21$ MeV) in the left P detector; θ_{pn} is the angle between the neutron and the proton directions. The ordinate is the number of neutron counts per unit solid angle for each detected proton. The data points are the experimental results, while the dashed line is the prediction of the Monte Carlo simulation based on the PWIA model.

Figure 10 shows the angular correlation between the detected neutrons and protons for the angular range covered by our detectors. The open triangles are the measured data points, while the dashed line shows the full Monte Carlo simulation, including all effects from multiple scattering and from angular and energy resolutions of both sets of detectors.

V. BACKGROUNDS

A. Beam contamination

As mentioned in Sec. II A, the muon beam contained a contamination of roughly 20% electrons. Since nearly every muon stopping in the target decayed under emission of an electron, the background rate from beam electrons was small compared to that from decay electrons (discussed in Sec. V C). Furthermore, the detection of any hadronic events induced by beam electrons was suppressed to an insignificant level by the prompt veto and the muon gate requirement.

The pion contamination, though small (<0.1%), was potentially more troublesome since nearly all negative pions are captured after stopping and produce energetic nucleons. In the case of pion capture on ^{3}He, the likelihood for the emission of a proton above 20 MeV is 19% and the likelihood for deuteron emission is 16% [28]. To produce a background event, a pion had to enter the target during an already open muon gate, since a pion opening its own gate would have captured or decayed within the 300 ns blanking time. In addition, to reach the ^{3}He target a pion needed a minimum momentum of 3 MeV/c above the mean beam momentum, which had a probability of only 1% due to the very narrow momentum tune. Taking all these factors into account we derive an upper limit of 5000 pions stopped in the target during any open muon gate throughout our experiment. The acceptance for events generated by these pions was considerably less than the 0.7–0.8 % for muon-induced events, since the pions were likely to stop early in the target. Taking 0.7% as an upper limit, and multiplying by 5000 and the above-mentioned proton emission probability of 20%, we estimate at most 6–7 pion capture events in our data sample. These events were suppressed by the prompt veto with an efficiency of at least 98% and can thus be completely disregarded.

B. Wall stops

Another possibly important background contribution comes from muons stopped in the target walls. Roughly 3% of all "good" muons (with proper signals in all beam counters) stopped in the target walls instead of the ^{3}He gas. Although this percentage is small, the capture rate on high Z material is so overwhelmingly larger than for Z=2 that this background could potentially swamp the desired signal. The Monte Carlo simulation predicted that the total proton rate in the P counters from wall stops should be roughly 30–40% of the rate from muon capture on ^{3}He. For the highest energy protons, as well as for deuterons that stop in P, the Monte Carlo calculation predicted an 8:1 ratio for background over good events.

Fortunately, this background was easily suppressed by the 300 ns blanking time at the beginning of each muon gate. During that time, all but 1.6% of the muons that stopped in the lead walls were captured, leaving a background-to-signal rate of less than 13% even for the highest energies (where the statistical error is significantly larger). This result agrees well with the measured decay time spectra; e.g., the deuteron spectrum is consistent with a (2±8)% background component with short lifetime. According to the Monte Carlo simulation, the muon stop rate in structural material other than lead was so small that the contribution from muon capture in these materials is completely negligible.

C. Michel electrons

Muon decay electrons that are mistaken for protons can make a direct contribution to the background rate. Since the electron rate exceeds that of high energy protons by a factor of 10^5, even a tiny fraction of misidentified electrons can lead to a sizable background contribution. We suppressed this background by using the veto counter VP (75% of all electrons reach VP), and requiring signals several times above minimum ionizing in at least two out of the three charged particle counters. Especially the Si counter provided a rather clean separation of electrons and heavier particles. Monte Carlo studies showed that the electron induced events were suppressed by at least a factor of 10^5 by these cuts. Any remaining electron events would be concentrated at about 3–4 ns below the main proton band and at small scintillator signal in the TOF spectrum (Fig. 5). Very few events are visible in that region, and the indicated software gate reduced this background to a negligible level.

A more indirect background contribution could come from interactions of the Michel electrons with target material. For an order-of-magnitude estimate of the proton rate from electron and photoproduction we considered the following simplified model. Each electron in our Monte Carlo simulation was followed through the target constituents (gas and walls), and bremsstrahlung photons produced by the electron were flagged (see Sec. III D). The likelihood of these photons knocking out a proton from intervening material was estimated from the experimental results of Ryckbosh *et al.* [30], and the protons produced were followed through the apparatus. It turned out that these kinds of events were strongly suppressed by the target-detector geometry and the rather low cross section for proton production at energies above the giant resonance region. The estimated upper limit for the number of events in our data set coming from this background is 0.1 events.

D. Charge exchange/pickup reactions

While all background contributions discussed so far turned out to be negligible, there was one source of background that led to a significant rate (28%) in the proton spectrum of the left detector arm. This background was evident in the decay time spectrum (see Sec. IV D) as well as the energy spectrum (events with too high energy, far beyond what we saw in the right detector arm).

A careful analysis of a number of special runs that were taken interspersed with the data runs showed that this background was associated with the primary proton beam, but not with the secondary beam in the experimental area nor with cosmic rays. We conclude that these background events were caused by neutrons produced by the primary beam that penetrated our apparatus from right to left, creating high-energy protons through charge exchange and knock-out reactions. This conclusion is supported by the fact that there was a path of minimal shielding from the production target to the right side of our apparatus. We also observed directly hadronic events going "backward," i.e., with a negative time of flight, in the right detector arm.

Since this kind of primary beam induced background is completely random in time (on the time scale of muon decay) we could remove it by subtracting the second half of each decay time spectrum from the first half (see Sec. IV D). The sample of deuteron events on the left side was too small to distinguish whether the same background was present or not, so we used the subtraction method for the left side high energy deuterons as well. For the coincident data, the background events in the left P detector were associated with a negative neutron time of flight and could thus easily be removed, without resorting to the subtraction method.

E. Accidental coincidences

Accidental coincidences between protons in the left charged particle detector arm and signals from uncorrelated neutrons or photons in the neutron counter are a possible background contribution to our *p-n* coincidence data. For such an accidental coincidence to be mistaken for a real *p-n* event, the time difference between the neutron signal and the proton signal would have to be within a 20 ns window. The total singles rate in the neutron counter was 7 kHz above the threshold of 3 MeV el. eq. The likelihood of an unrelated signal occurring in the neutron counter during a 20 ns window was thus 1.4×10^{-4} for each proton event. Since the total number of proton events in the left detector arm was about 730, the expectation value for the number of false coincidences throughout our run is 0.1 events, which can be neglected. This result is supported by the fact that we see no *p-n* events with "unphysical" neutron energies (i.e., velocities between 35% and 100% of the speed of light).

VI. RESULTS

A. Proton spectra

Our final proton energy spectrum is shown in Fig. 8, which gives the partial capture rate, averaged over 5 MeV bins, as a function of proton energy. The circular data points are from the right detector arm and were extracted from the data as described in Sec. IV D. The triangular points are from the left detector arm data; they have larger error bars due to the background subtraction applied to these data. The error bars shown are statistical only; both data sets have an overall normalization uncertainty of ±10% each (the normalization could be different for the two detector arms, due to different solid angles and detector responses). Within statistical uncertainties, the two data sets agree with each other (the χ^2 is 2 per degree of freedom without renormalization, and 1.2 if one changes the overall relative normalization of the two data sets by 10%). Table I gives the numerical values for all data points shown in Fig. 8.

The dashed curve shown in Fig. 8 is the initial energy spectrum that we used as input to our model calculation (see Sec. III C), without any adjustable parameters. This model spectrum describes the data rather well (see also Fig. 7), which is probably somewhat fortuitous. A more realistic calculation would have to include a microscopic wave function for the initial-state, final-state interactions, and effects from meson exchange contributions. Our coincidence results show that our model does not describe all aspects of the three-body breakup data (see below), so that one should not take the agreement with the inclusive proton data (Fig. 8) too seriously.

We compare the present results with earlier measurements on proton emission in extreme kinematics following nuclear muon capture on selected heavier nuclei [14,31]. For this purpose we calculate the fraction of all muon capture events leading to the emission of a proton above some threshold energy E_{thresh}. We chose the threshold energy in the range 42–45 % of the maximum possible proton energy $E_{\max}$ allowed by kinematics. The results of this comparison are shown in Table II. While the absolute muon capture rate increases steeply with Z, it is evident from Table II that the fraction of muon captures leading to proton emission in extreme kinematics is largest for light nuclei.

B. Proton-neutron coincidences

As described in Sec. IV F, our neutron data are rather limited, thereby restricting the possibilities for a statistically meaningful analysis. Nevertheless, we used these data to gain some more insight into the reasons for the rather good agreement between simulated and measured inclusive proton energy spectra.

Figure 10 shows the data (triangles) for the number of observed coincident neutron-proton events having proton energies above 21 MeV and neutron energies above 10 MeV. The data are plotted as a function of $\cos\theta_{pn}$, where θ_{pn} is the angle between the proton and neutron directions (see Sec. IV F). The angular distribution in Fig. 10 is influenced strongly by the finite geometry of the two detector systems (neutron detector and left-side charged particle telescope) which are fixed at a relative

TABLE I. Partial muon capture rates for proton emission. The rate is given by $d\Gamma/dE_p$ with standard deviation σ_Γ. The R and L designate right and left detector arms, respectively. The energy E_p gives the centroid of each 5 MeV bin.

E_p(mean) (MeV)	$d\Gamma/dE_p$(R) (MeV^{-1} s^{-1})	σ_Γ(R) (MeV^{-1} s^{-1})	$d\Gamma/dE_p$(L) (MeV^{-1} s^{-1})	σ_Γ(L) (MeV^{-1} s^{-1})
17.0	1.787	0.176	1.589	0.397
22.0	0.749	0.039	0.965	0.102
27.0	0.338	0.022	0.440	0.055
32.0	0.156	0.014	0.238	0.036
37.0	0.0728	0.0096	0.0804	0.0278
42.0	0.0195	0.0045	0.039	0.0203
47.0	0.0037	0.0023	—	—
52.0	0.0035	0.0024	—	—

TABLE II. Fraction of muon captures by selected nuclei leading to high energy proton emission between $E_{\rm thresh}$ and $E_{\rm max}$.

Target	$E_{\rm max}$ (MeV)	$E_{\rm thresh}$ (MeV)	$E_{\rm thresh}/E_{\rm max}$ (%)	$\Gamma_{E>E_{\rm thresh}}/\Gamma_{\rm tot}$ (10^{-4})
^{3}He	63.9	27	42	10.0±1.0
^{12}C	70.9	30	42	3.24±0.06
^{40}Ca	92.7	40	43	2.32±0.02
^{89}Y	88.2	40	45	0.72±0.02

angle of about 180°; e.g., the spectrum cuts off rapidly for $\theta_{pn} < 154°$ ($\cos\theta_{pn} > -0.9$). Instead of trying to extract an "undistorted" angular distribution from these data, we have started from the result for three-body breakup into $p + n + n$ in the PWIA model (Sec. III C) and obtained the Monte Carlo angular distribution taking into account the experimental geometry, multiple scattering, and detector resolution. This calculation is shown by the dashed line in Fig. 10.

In the region $-1.0 < \cos\theta_{pn} < -0.9$ we can make qualitative comparisons between the data (two points) and the model calculation. It seems that the data are distributed more isotropically than the model prediction which rises sharply toward $\theta_{pn} = 180°$. Also, the observed number of coincidences (29) is lower than the predicted number (39) by 1.5 standard deviations. This is again consistent with a relatively flat angular distribution, where more neutrons than predicted are emitted at angles less than 154° and thus miss the neutron detector. In such cases, momentum conservation requires that the second (unobserved) neutron carry away substantial momentum.

Further support for this conclusion comes from an analysis of the root-mean-square value of the missing momentum $\sqrt{\langle p^2_{\rm miss}\rangle}$. The model prediction for this value is 88.7±2.2 MeV/c, while the experimental data yield $\sqrt{\langle p^2_{\rm miss}\rangle} = 110 \pm 6.5$ MeV/c (3 standard deviations higher). A comparison between the input spectrum of our PWIA model and the Monte Carlo result shows that this quantity is an unbiased estimator for the true root-mean-square missing momentum, averaged over the kinematic regime limited by $E_p > 21$ MeV, $E_n > 10$ MeV, and $\cos\theta_{pn} < -0.875$. The fact that the experimental value is higher confirms that substantially more momentum (and thus energy) is transferred to the unobserved neutron than our model predicts (the momentum transferred to the neutrino is small compared to the numbers quoted above). One possible explanation would be that the high-momentum protons we observe are mainly spectators, while the muon captures predominantly on a p-n pair inside the ^{3}He nucleus, transferring a substantial amount of energy to both final state neutrons. This agrees with the dominance of p-n capture over p-p capture observed in pion absorption in ^{3}He [28]. Obviously, more data are needed to corroborate this speculation.

C. Deuteron spectra

Figure 9 shows our final deuteron energy spectrum in terms of the partial capture rate per energy bin. The low energy data point (triangle) comes from the dP-detector data in the left spectrometer arm, while the two high-energy points are the data from the right arm P detector (solid circle) and the background subtracted data from the left P detector (triangle), respectively. The method by which these results were extracted from the data is described in Sec. IV E. The numerical values for all data points are given in Table III.

The dashed line shown in Fig. 9 is the initial energy spectrum from our model calculation without adjustable parameters (as for the proton spectrum). Although the same model describes the proton data reasonably well, it lies below the deuteron data by a large factor. We also performed a more sophisticated PWIA calculation of the deuteron spectrum (solid line in Fig. 9; see below). This calculation agrees better with the data, but still underpredicts the high energy data points. We consider this as further evidence for the presence of additional capture strength beyond that given by the one-nucleon impulse approximation.

The model of Bernabéu, Ericson, and Jarlskog [18] can be used to estimate the capture strength at high energy transfer (Sec. I). While their approach is only valid at the kinematic end point (E_ν=0), we attempted a crude comparison of our deuteron data with a prediction based on their method. For that purpose we fitted our data to a function

TABLE III. Partial muon capture rates for deuteron emission. See Table I for explanation of symbols.

E_d (MeV)	$d\Gamma/dE_d$(R) (MeV^{-1} s^{-1})	σ_Γ(R) (MeV^{-1} s^{-1})	$d\Gamma/dE_d$(L) (MeV^{-1} s^{-1})	σ_Γ(L) (MeV^{-1} s^{-1})
19.8±0.57	—	—	0.751	0.052
28.0±0.53	0.072	0.019	—	—
28.4±0.53	—	—	0.048	0.025

$$d\Gamma/dE_d$$

$$= C_0(E_{d\,\max} - E_d)^2 \exp(-C_1[E_{d\,\max} - E_d]) \ , \quad (5)$$

where the factor $(E_{d\,\max} - E_d)^2$ is proportional to the neutrino phase space. Extrapolating to the kinematic end point at $E_\nu = 0$, which corresponds to $E_d = E_{d\,\max} = 33.6$ MeV, we find that our data are consistent with

$$d\Gamma(^3\text{He} + \mu^- \rightarrow d + n + \nu_\mu)_{E_\nu \rightarrow 0}$$

$$= (6.0 \pm 1.5) \times 10^{-5}\ \text{s}^{-1} \frac{E_\nu^2 dE_\nu}{[\text{MeV}^3]} \ . \quad (6)$$

On the other hand, Eq. (20) in Ref. [18] yields the value $(59{\pm}21) \times 10^{-5}\ \text{s}^{-1}$ for the numerical constant in Eq. (6), after summing over both two-body and three-body final states. (To arrive at this result we used the experimental results of Schwanner *et al.* [32] and the prescription of Khankhasayev [33] to extract the *p*-wave scattering volume from these data, see Sec. I.) Comparing these two values (6.0±1.5 and 59±21) one concludes that they are consistent if 6–16 % of all muon capture events at the kinematic limit lead to the emission of a deuteron. This fraction compares well with the observed deuteron emission probability of 16% in *pion* capture on ^{3}He [28], which is related to the corresponding deuteron emission process in *muon* capture within the framework of the Bernabéu *et al.* model. Within the uncertainties of that model and our extrapolation this good agreement points to the importance of two-nucleon currents in the capture operator; such currents are dominant in pion capture and thus automatically included in the prediction of muon capture rates following the approach of Ref. [18].

D. PWIA calculation for the deuteron channel

To further corroborate the significance of the excess capture strength observed in the emission of high energy deuterons, a more rigorous calculation of the deuteron spectrum was performed in PWIA. The strong interaction between the deuteron and the neutron in the final state was ignored, the current was taken to be due to the nucleonic degrees of freedom only, and only the direct nucleon knock-out amplitude was included. Because of these approximations, the deuteron spectrum can be cast into a simple form (see also Sec. III C):

$$\frac{d\Gamma}{dE_d} = \gamma \rho_2(p_d) \langle |M|^2 \rangle \ , \quad (7)$$

where γ is a kinematical factor, $\rho_2(p_d)$ is the two-body breakup momentum distribution evaluated at the deuteron momentum p_d, and $\langle |M|^2 \rangle$ is the squared average transition matrix element for the elementary process on the proton.

The two-body breakup momentum distribution was calculated using the 22 channel ^{3}He wave function of Kameyama *et al.* [34], with a binding energy of 7.76 MeV and the deuteron wave function taken from the Bonn potential *C* [35]. Our theoretical values for $\rho_2(p_d)$ exceed the result for the "experimental spectral function" $S(p_{\text{miss}} = p_d)$ [27] by factors up to 2.4 at the high deuteron-energy end of the spectrum. It should be noted that the experimental values for $S(p_{\text{miss}})$ of Ref. [27] come from derivations from electron scattering cross sections that assume the validity of PWIA and are thus subject to large corrections from final-state interactions (FSI) and MEC, as has been pointed out by Laget [36,37].

The matrix element squared was found by contracting lepton and nucleon current-current tensors with standard trace techniques. We evaluated the matrix element for two different approximations, referred to in the following as "PWIA ON" and "PWIA OFF." For PWIA ON, the spinor of the struck proton was taken to obey the Dirac equation for a free particle, with energy set by its three-momentum according to

$$E_p(\mathbf{p}_p) = (\mathbf{p}_p^2 + m_p^2)^{1/2} \ . \quad (8)$$

For PWIA OFF, the energy of the struck proton was set equal to $p_0 = M(^3\text{He}) - E_d(\mathbf{p}_d)$ and the spinor was taken to obey the following "quasifree Dirac equation":

$$\gamma^\mu p_\mu u_p(\mathbf{p}) = W u_p(\mathbf{p}) \ . \quad (9)$$

In Eq. (9), the effective mass W is given by $W^2 = p_0^2 - \mathbf{p}^2$. The dependence of the off-shell form factors on the deviation of W from m_p was ignored. The quantity $\delta = 1 - W/m_p$, which is a measure of how far "off-shell" the proton is, varies from 0.6 to 12 % as E_d varies from its lowest to its highest value.

Our result for the total capture rate was 1583 sec^{-1} for PWIA ON and 1627 sec^{-1} for PWIA OFF, roughly a factor of 4 higher than the value found by Phillips *et al.* [38] who included FSI using the Amado model. At low deuteron energies, which dominate the total capture rate, FSI effects are large and the PWIA is expected to be poor. In fact, the spectrum found using the PWIA peaks at $E_d = 1.2$ MeV, at which point the deuteron-neutron c.m. kinetic energy lies between zero and 12 MeV, so that FSI should have a very large effect. As the deuteron energy increases the neglect the FSI becomes a better approximation (for $E_d = 16$ MeV the deuteron-neutron c.m. kinetic energy is between 32 and 59 MeV). The PWIA OFF differential rate is higher than the PWIA ON differential rate for all E_d and the enhancement increases up to a factor 3.6 at the high energy end point of the deuteron spectrum. At $E_d{=}28$ MeV (our highest measured energy) the enhancement is 1.7. The calculated deuteron spectrum above $E_d{=}16$ MeV for PWIA OFF is shown as the solid line in Fig. 9.

While this PWIA calculation reproduces rather well the data point at moderate deuteron energy, it still is too low at the highest energies. Using the PWIA OFF result as input to our Monte Carlo, we get an expected counting rate in the P detectors that is lower than the data by a factor of 2.5 (or 2.3 standard deviations), suggesting additional contributions from two-body currents.

Clearly, though, as a next step FSI must be included in a calculation before any firm conclusions above the contributions of MEC or other two-body effects can be drawn.

VII. SUMMARY

We report in this paper the first measurement of kinematic variables for the final-state nuclear fragments of ^{3}He after nuclear muon capture leading to two-body and three-body breakups. These data extend the existing data set on high-energy proton emission after muon capture from heavier targets down to $Z = 2$. They confirm the occurrence of nuclear muon capture in extreme kinematics throughout the periodic table. Comparison of our data with several simple models favors the interpretation that capture events with large energy transfer to the nucleus involve more than one nucleon, e.g., pair capture, meson exchange currents, etc. To determine unambiguously the origin of these high energy transfer events, one has to compare our data to fully microscopic calculations that take these multinucleon effects into account. We hope our data will stimulate such calculations, which are now becoming feasible in the $A = 3$ system.

ACKNOWLEDGMENTS

We wish to thank C. J. Martoff, N. C. Mukhopadhyay, and H. W. Fearing for valuable discussions. We gratefully acknowledge the Pew Foundation for providing the computer facility used in the analysis of this work. We also thank the entire staff at TRIUMF, particularly W. Kellner and D. C. Healey, for their generous help in carrying out the experiment. Our special thanks go to Jack Walton at LBL who built the silicon detectors used in this experiment. The research was supported in part by the U.S. National Science Foundation and the Natural Sciences and Engineering Research Council of Canada (NSERC).

[1] L. L. Foldy and J. D. Walecka, Nuovo Cimento **34**, 1026 (1964).

[2] N. C. Mukhopadhyay, Phys. Rep. **30C**, 1 (1977).

[3] J. S. O'Connell, T. W. Donnelly, and J. D. Walecka, Phys. Rev. C **6**, 719 (1972).

[4] F. Dautry, M. Rho, and D. O. Riska, Nucl. Phys. **A264**, 507 (1976).

[5] J. van der Pluym, T. Kozlowski, W. H.A. Hesselink, A. van der Schaaf, Ch. Grab, E. A. Hermes, and W. Bertl, Phys. Lett. B **177**, 21 (1986).

[6] A. van der Schaaf, E. A. Hermes, R. J. Powers, F. D. Schlepütz, R. G. Winter, A. Zglinski, T. Kozlowski, W. Bertl, F. Felawka, W. H. A. Hesselink, and J. van der Pluym, Nucl. Phys. **A408**, 573 (1983).

[7] T. Kozlowski, W. Bertl, H. P. Povel, U. Sennhauser, H. K. walter, A. Zglinski, R. Engfer, Ch. Grab, E. A. Hermes, H. P. Isaak, A. van der Schaaf, J. van der Pluym, and W. H. A. Hesselink, Nucl. Phys. **A436**, 717 (1985).

[8] E. K. McIntyre, T. J. Hallman, K. S. Kang, C. W. Kim, Y. K. Lee, L. Madansky, and G. R. Mason, Phys. Lett. **137B**, 339 (1984).

[9] Y. G. Budyashov, V. G. Zinov, A. D. Konin, A. I. Mukhin, and A. M. Chatrchyan, Zh. Eksp. Teor. Fiz. **60**, 19 (1971) [Sov. Phys. JETP **33**, 11 (1971)].

[10] M. P. Balandin, V. M. Grebenyuk, V. G. Zinov, T. Kozlowski, and A. D. Konin, Yad. Fiz. **28**, 582 (1978) [Sov. J. Nucl. Phys. **28**, 297 (1978)].

[11] K. S. Krane, T. C. Sharma, L. W. Swenson, D. K. McDaniels, P. Varghese, B. E. Wood, R. R. Silbar, H. D. Wohlfahrt, and C. A. Goulding, Phys. Rev. C **20**, 1873 (1979).

[12] G. E. Belovitskii *et al.*, Yad. Fiz. **43**, 1057, (1986) [Sov. J. Nucl. Phys. **43**, 673 (1986)].

[13] C. J. Martoff, D. Počanić, L. W. Whitlow, S. S. Hanna, H. Ullrich, S. Cierjacks, M. Furić, T. Petković, and H. J. Weyer, Czech. J. Phys. B **36**, 378 (1986).

[14] C. J. Martoff, W. J. Cummings, D. Počanić, S. S. Hanna, H. Ullrich, M. Furić, T. Petkovi c, T. Kozlowski, and J. P. Perroud, Phys. Rev. C **43**, 1106 (1991).

[15] H. Paganetti, P. David, H. Hänscheid, J. Konijn, C. T. A. M. de Laat, W. Lourens, F. Risse, Ch. Rösel, L. A. Schaller, and A. Taal, Z. Phys. A **343**, 113 (1992).

[16] Y. K. Lee, T. J. Hallman, L. Madansky, S. Trentalange, G. R. Mason, A. J. Caffrey, E. K. McIntyre, Jr., and T. R. King, Phys. Lett. B **188**, 33 (1987).

[17] M. Lifshitz and P. Singer, Nucl. Phys. **A476**, 684 (1988).

[18] J. Bernabéu, T. E. O. Ericson, and C. Jarlskog, Phys. Lett. **69B**, 161 (1977).

[19] B. Goulard, N. Lorazo, and H. Primakoff, Phys. Rev. C **26**, 1237 (1982).

[20] M. Doi, T. Sato, H. Ohtsubo, and M. Morita, Nucl. Phys. **A511**, 507 (1990).

[21] W. J. Cummings, G. E. Dodge, S. S. Hanna, B.H. King, S. E. Kuhn, Y. M. Shin, R. Helmer, R. B. Schubank, N. R. Stevenson, U. Wienands, Y. K. Lee, G. R. Mason, B. E. King, K. S. Chung, J. M. Lee, and D. P. Rosenzweig, Phys. Rev. Lett. **68**, 293 (1992).

[22] W. Glöckle, H. Witala, and Th. Cornelius, Nucl. Phys. **A508**, 115 (1990).

[23] R. Abegg *et al.*, Nucl. Instrum. Methods **A234**, 20 (1985).

[24] *TRIUMF Kinematics Handbook*, edited L. G. Greeniaus (TRIUMF, Vancouver, Canada, 1987).

[25] S. E. Kuhn and G. E. Dodge, Nucl. Instrum. Methods **A322**, 88 (1982).

[26] R. A. Cecil, B. D. Anderson, and R. Madey, Nucl. Instrum. Methods **161**, 439 (1979).

[27] E. Jans, M. Bernheim, M. K. Brussel, G. P. Capitani, E. De Sanctis, S. Frullani, F. Garibaldi, J. Morgenstern, J. Mougey, I. Sick, and S. Turck-Chieze, Nucl. Phys. **A475**, 687 (1987).

[28] D. Gotta, M. Dörr, W. Fetscher, G. Schmidt, H. Ullrich, G. Backenstoss, W. Kowald, I. Schwanner, and H.-J. Weyer, Phys. Lett. **122B**, 129 (1982).

[29] N. L. Johnson and F. C. Leone, *Statistics and Experimental Design* (Wiley, New York, 1964), p. 41.

[30] D. Ryckbosh, L. van Horrebeke, R. Van de Vyver, F. De Smet, J.-O. Adler, D. Nilsson, B. Schröder, and R. Zorro, Phys. Rev. C **42**, 444 (1990).
[31] W. J. Cummings, Ph.D. thesis, Stanford University, 1991.
[32] I. Schwanner, G. Backenstoss, W. Kowald, L. Tauscher, H.-J. Weyer, D. Gotta, and H. Ullrich, Nucl. Phys. **A412**, 253 (1984).
[33] M. Kh. Khankhasayev, Nucl. Phys. **A505**, 717 (1989).
[34] H. Kameyama, M. Kamimura, and Y. Fukushima, Phys. Rev. **40**, 974 (1989).
[35] R. Machleidt, Adv. Nucl. Phys. **19**, 189 (1989).
[36] L. M. Laget, Can. J. Phys. **62**, 1046 (1984).
[37] L. M. Laget, Phys. Lett. **151B**, 325 (1985).
[38] A. C. Phillips, F. Roig, and J. Ros, Nucl. Phys. **A237**, 493 (1975).

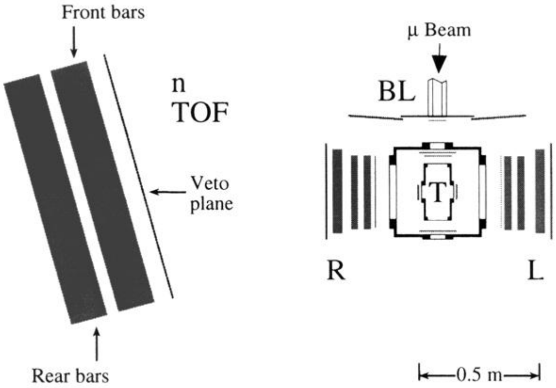

FIG. 1. Overview of the experimental setup. This figure shows the relative spatial arrangement of the beam line (BL), target (T), left (L), and right (R) charged particle telescopes, and the neutron time-of-flight detector (n TOF).